CrossMark

Thermographic and tomographic methods for tridimensional characterization of thermal transfer in silica/phenolic composites

G. Bresson [a, b], A. Ahmadi-Sénichault [a], O. Caty [b], V. Ayvazyan [a], M.L. Gregori [c], S.F. Costa [c], G.L. Vignoles [b, *]

[a] I2M, Université de Bordeaux, Arts et Métiers ParisTech, CNRS, Talence, France
[b] LCTS, Université de Bordeaux, UMR 5801 CNRS, Herakles, CEA, Pessac, France
[c] CTA/IAE, S. José dos Campos, SP, Brazil

ABSTRACT

Silica/phenolic composite materials are often used in thermal protection systems (TPS) for atmospheric re-entry. The present work aims to compare two different approaches to assess heat transfer properties of these materials: i) using standard and specific experimental methods, and ii) with the development of 3D thermal transfer multiscale model using 2D (microscopy) and 3D (tomography) images. The latter procedure, based on computations on images, is a two-step change of scale from microscopic scale to mesoscopic scale and then to the macroscopic one. Two silica/phenolic composites with different spatial organizations are studied and their thermal properties are compared. Several experimental methods have been used, including space-resolved diffusivity determinations. Numerical results are compared to experimental ones in terms of transverse and longitudinal thermal conductivities of the composites, and were found to be in good agreement. A discussion is made on the different possible sources of uncertainty for both methods.

© 2016 Elsevier Ltd. All rights reserved.

1. Introduction

The development of new composites with low weight and high performance is an important issue for the production of thermal protection systems (TPS) for atmospheric re-entry of space objects [1]. Among them, silica-phenolic composites have shown excellent thermal performances [2], and very good ablation resistance [3,4]. In order to reduce processing costs and to optimize the material with respect to its mission, recent works [5,6] have focused on the fabrication and characterization of composites in which the reinforcement is in the form of discontinuous chopped fabric pieces. This kind of improvement has been studied on aramid/epoxy composites [7], and more generally on polymer-matrix composite prepregs for damage tolerance through mechanical testing [8]. The result is an elimination of the tendency of the material to delaminate [5], as compared to the same material with 2D continuous fabric layup reinforcement, but at the expense of some abatement in mechanical properties like stiffness [9].

In this paper, we focus on the determination of the thermal properties for this class of materials, comparing the « chopped » arrangement to the continuous fabric layup. Two approaches will be developed in parallel and compared to each other. First, thermal measurements are performed by flash, hot disk and DSC methods. Second, the material structure assessed by microscopy and tomography and the properties of the components are used in an *ad-hoc* numerical procedure to predict the effective thermal diffusivity of the composite. The simultaneous development of these methods aims to contribute to the creation of a «material design tool» which can predict the influence of the reinforcement architecture on the effective thermal diffusivity or conductivity of the composite.

The materials and methods are first described; then, results from the thermographic and tomographic methods are presented and discussed.

2. Materials

The studied material samples were processed by Plastflow Ltd, Curitiba, Brazil, from a regular fabric, about 0.9 mm thick, of pure silica with an areal mass of 680 g/m^2 and a phenolic resin with

Nomenclature

	λ	Thermal conductivity (W m^{-1} K^{-1})
	$\underline{\underline{\lambda}}$	Local thermal conductivity tensor of a sub-block (W m^{-1} K^{-1})
Roman letters	$\underline{\underline{\lambda}}^*$	Macroscopic thermal conductivity tensor of a composite (W m^{-1} K^{-1})
a — Thermal diffusivity (m^2 s^{-1})	λ_f	Thermal conductivity of the fibers (W m^{-1} K^{-1})
c_p — Mass thermal capacity (J K^{-1} kg^{-1})	λ_m	Thermal conductivity of the matrix (W m^{-1} K^{-1})
d — Dimension of the problem (−)	$\lambda_{//}^*$	Longitudinal macroscopic thermal conductivity of a composite (W m^{-1} K^{-1})
F — Conductivity contrast factor, $(\lambda_m + \lambda_f)/(\lambda_m - \lambda_f)$		
N1 — Threshold gray scale value	$\lambda_{\perp}^*$	Transverse macroscopic thermal conductivity of a composite (W m^{-1} K^{-1})
N2,N3 — Gray scale values used for density/gray scale correspondence	$\lambda_{//}$	Thermal conductivity of a yarn parallel to the fibers (W m^{-1} K^{-1})
S_{xi} — Normalized sensitivity of λ^* to the variation of x$_i$	$\lambda_{\perp}$	Thermal conductivity of a yarn perpendicular to the fibers (W m^{-1} K^{-1})
Greek letters	ρ	Density (kg m^{-3})
ϕ_f — Volume fraction of fibers	τ	Parameter quantifying thermal anisotropy
$\phi_{f,yarn}$ — Volume fraction of fibers in a yarn		
ϕ_m — Volume fraction of the matrix		
$\phi_{m,yarn}$ — Volume fraction of the matrix in a yarn		

165 mPa s viscosity, used at room temperature to obtain the prepreg material [6]. Two configurations of the silica fiber reinforcement were studied (Fig. 1). The first one is obtained by simply stacking the as-received prepreg layers, while the other one was made from the same prepregs, but in a chopped form. The "chopped fabric" composite is composed of a random arrangement of small, approximately square pieces of prepreg with an edge size of 20–28 mm. The two kinds of reinforcements are placed in
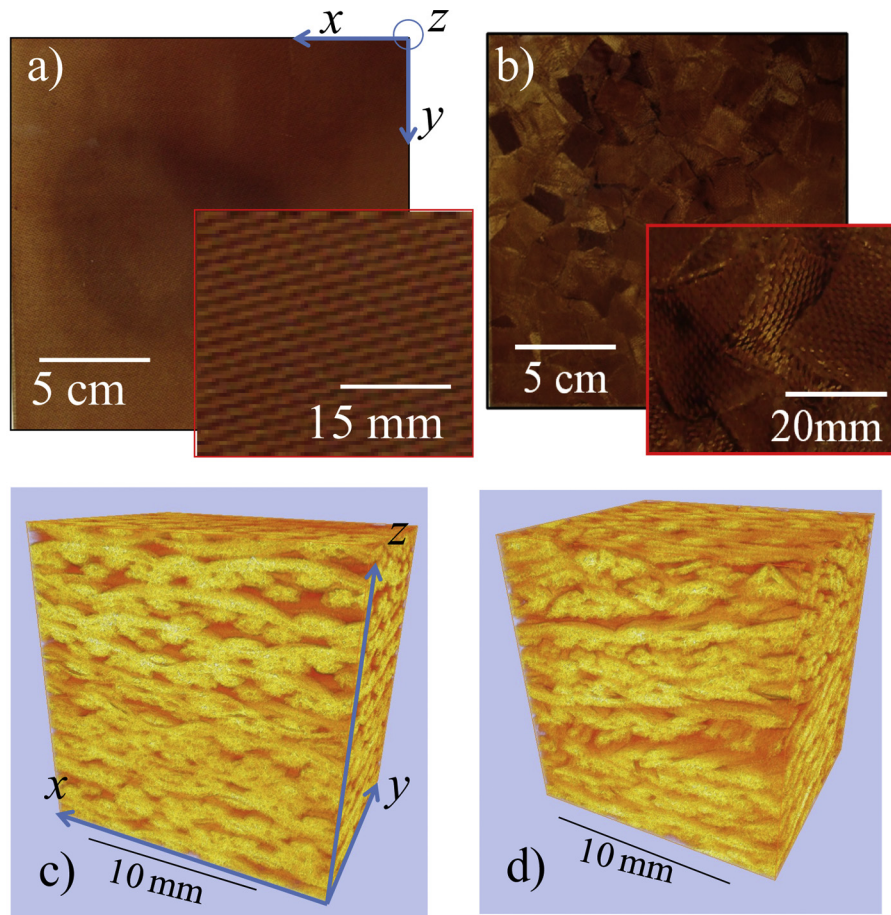
Fig. 1. Photographs of the studied materials: a,c) regular composite; b,d) chopped composite. a,b) Full samples and zooms on the textures. c,d) 3D renderings of μCT data at 5 μm pixel size (resp. 346 × 274 × 354 pixels and 284 × 325 × 340 pixels). The orange tones in the top figures are actual resin colors, while they are artificial colors in the X-ray CT renderings, linked to the X-ray effective absorption coefficient (bright = high absorption, orange/transparent = low absorption). (For interpretation of the references to colour in this figure legend, the reader is referred to the web version of this article.)

multilayer configurations to obtain plates. Then, a hot compression process (15 min/70 bar/175 °C) and a second cure are applied to both materials (12 h/1 atm/180 °C). The final dimensions are $240 \times 240 \times 8$ mm^3.

3. Experimental methods

3.1. Properties of the components

Individual components were tested and data are reported in Table 1. Density measurements were made with an Accupyc 1330 He pycnometer; the results are consistent with ref. [5]. The fiber average diameter was estimated using microscopic observations on approximately 350 fibers. The matrix thermal properties were obtained using flash thermography (diffusivity) and DSC (heat capacity). The fiber heat capacity was obtained by subtraction between the composite and the matrix values, and its diffusivity by a specific laser excitation method [10]. The reported values will be used in the numerical computations based on tomographic images.

For each composite, the analysis of phase ratios was performed using Hg porosimetry (open porosity, skeletal density, and bulk density), combined to 3D (X-ray tomography) and 2D (optical microscopy) imaging. The results are synthesized in Table 1.

3.2. Thermal methods

Thermal analyses were done to obtain conductivities to validate numerical results. These values are also used to compare materials thermal behaviors. Firstly, an infrared thermographic analysis by a flash method was performed to experimentally measure the thermal diffusivity field (a) of the plates averaged through their thickness. The thermal diffusivity is essential to determine the thermal conductivity (λ) when the mass thermal capacity (c_p) and the density (ρ) are known, since a is $\lambda/\rho c_p$. This method consists in applying a photothermal pulse — the flash — on the front face of the material and measuring the evolution of the temperature on the rear face. The technique described by Degiovanni et al. [11] has been found more appropriate than the traditional method of Parker et al. [12], because of non-negligible thermal losses; it has been applied here on IR camera data for both composite samples, in both directions, and for the pure matrix. The average of the camera-recorded thermal field was used as the signal to be processed. It should be noted that the direction perpendicular to the composite plates will be called transverse, while those parallel to the plate will be called longitudinal.

The experimental setup is composed of a flashlight device (Elinchrom Style RX1200) acting on the front face of the composite sample and an IR camera (FLIR SC7000, 320×256 pixels) recording periodically (25 Hz) thermal images on the rear face. Adiabatic conditions were ensured on the sample sides by inserting them inside a PS foam holder. The flash impulsion is spread on the entire front face (30×30 mm^2) so as to place the sample in 1D heat transfer conditions. All samples being semi-translucid, their flashed face was painted in black.

The hot disk method [13,14] was also used to validate the values measured by thermography and to obtain the thermal conductivities in the principal directions. The measurements were performed with a TPS 2500 device by Hot Disk AB (Sweden).

DSC measurements were carried out on a Setaram Labsys™ 131 Evo apparatus, with a 5 °C/min heating rate, between ambient temperature and 110 °C.

4. Calculations

The model used to calculate the diffusivity and conductivity is based on 2D/3D image analysis and on a double change of scale. The method is described in Ref. [19] for a fibrous C/C composite but is also efficient for a large number of fibrous composites when μCT images of the material at different scales are available.

4.1. Imaging

The arrangement of fibers, pores and matrix, responsible of the specific thermal properties of the composites, exhibits two scales of heterogeneity that must be analyzed successively. They are illustrated in Fig. 2. Standard micrographic imaging of transverse sections of yarns (Fig. 2d) is sufficient to extract the structural information at this scale, the fibers being mostly parallel to each other. The low-resolution images (Fig. 2a−c) provide information only on the weaving pattern in the representative elementary volume (REV), but a 3D information is needed for accuracy; therefore, X-ray tomographs have been also used.

Micrographs were acquired on a standard optical microscope (Nikon Eclipse ME600) and a numerical microscope (Keyence VHX-1000). The ×50 magnification was optimal to analyze the fibers and was mostly used in this study. Several samples were cut in the plates and mechanically polished for observation. The micrographs were numerically acquired and the fibers and matrix components were separated by simple thresholding, followed by the application of a watershed algorithm, using ImageJ [15].

X-ray Microscale Computerized Tomographs (μCT) [16] were acquired using a laboratory device (Phoenics X-ray Nanotom) used

Table 1
Summary of various properties of the components and of the composites densities and phase fractions. All fractions are given with respect to the whole composite volume except the last two lines.

Quantity	Fibers	Matrix
Density (g cm^{-3})	2.21 ± 0.01	1.24 ± 0.01
Diameter (average) (μm)	8.6 ± 0.1	−
Heat capacity at 25 °C (J g^{-1} K^{-1})	0.83 ± 0.01	1.40 ± 0.01
Heat conductivity at 25 °C (W m^{-1} K^{-1})	1.40 ± 0.05	0.20 ± 0.01
Heat diffusivity at 25 °C (mm^2 s^{-1})	0.76 ± 0.03	0.11 ± 0.01
	Regular composite	**Chopped composite**
Skeleton density (kg/m^3)	1710 ± 10	1670 ± 10
Effective density (kg/m^3)	1590 ± 10	1570 ± 10
Open porosity	$6.5\% \pm 0.5\%$	$6.1\% \pm 0.5\%$
Fiber fraction	$45.3\% \pm 0.5\%$	$42.4\% \pm 0.5\%$
Matrix fraction	$48.1\% \pm 0.5\%$	$51.6\% \pm 0.5\%$
Yarn fraction	$69.5\% \pm 0.5\%$	$64.9\% \pm 0.5\%$
Extra-yarn matrix fraction	$25.0\% \pm 0.5\%$	$28.0\% \pm 0.5\%$
Intra-yarn matrix fraction	$34.7\% \pm 0.5\%$	$34.7\% \pm 0.5\%$
Intra-yarn fiber fraction	$65.4\% \pm 0.5\%$	$65.3\% \pm 0.5\%$
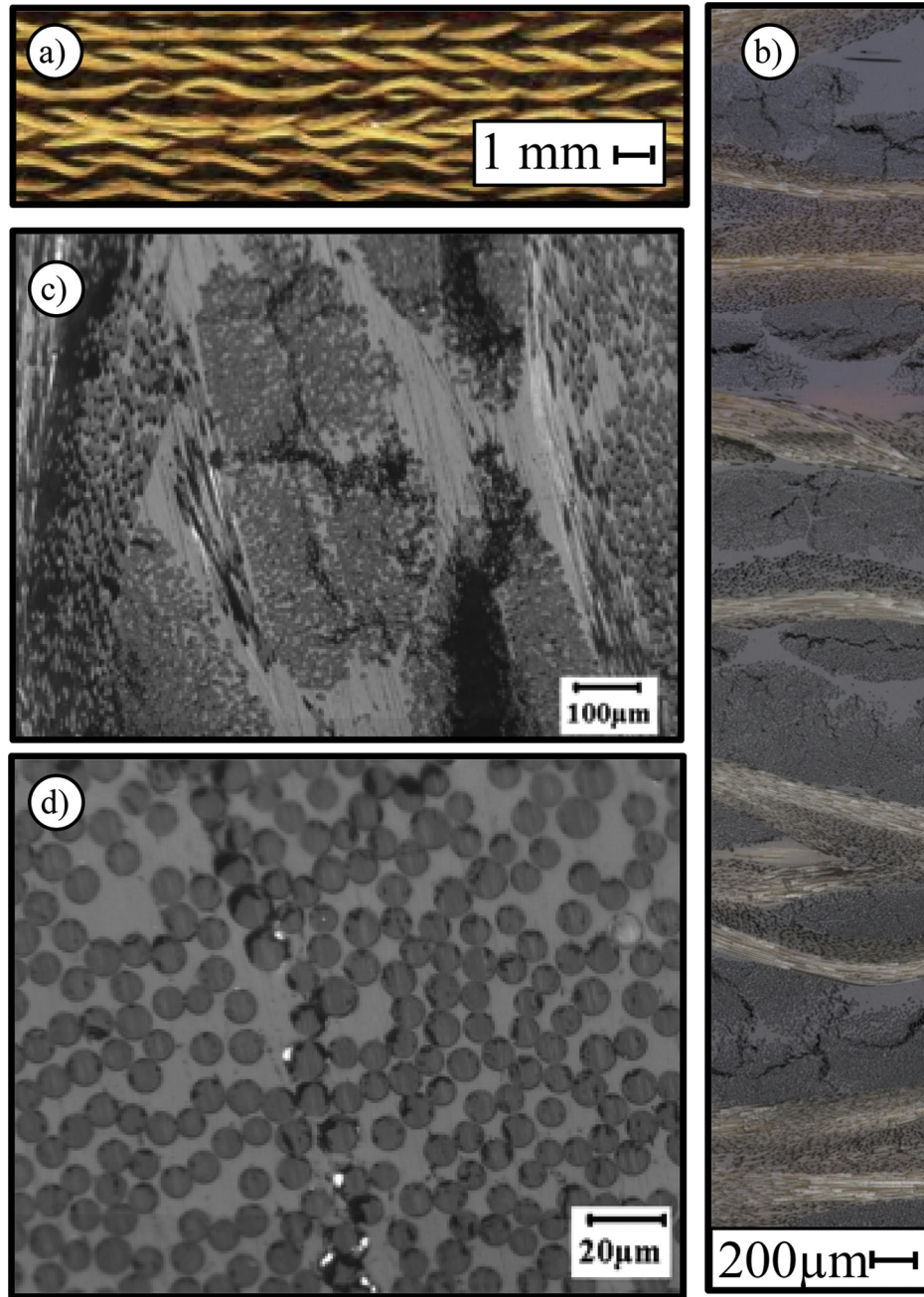
Fig. 2. Scale heterogeneity evidences with a) macroscopic, b,c) mesoscopic and d) microscopic scale of the regular composite. All images are optical micrographs.

in absorption mode with a resolution of 5 μm/pixel. The samples were extracted from the initial composite plate to be fully contained in the field of view at the resolution attempted. Reconstruction from the radiographs was performed by the standard filtered back-projection algorithm [17,18]. Examples of 3D μCT reconstructions are presented in Fig. 1c,d.

4.2. First change of scale based on 2D imaging

Knowledge of the detailed geometry and of the thermal properties of the components (fibers, matrix) of the composites is necessary to perform the first change of scale. For this, 2D micrographs taken perpendicularly to the yarn direction have been used. The assumption made is that the yarn is assumed to be unidirectional at this scale (*i.e.* the perpendicular pattern remains unchanged through the third direction). The parallel thermal conductivity ($\lambda_{//}$) is therefore simply obtained by a law of mixtures given by the following expression:

$$\lambda_{//} = \phi_f \lambda_f + \phi_m \lambda_m \tag{1}$$

where ϕ_f and ϕ_m are respectively the volume ratio of fibers and of the matrix in the material. λ_f and λ_m are respectively the conductivities of fibers and the matrix.

For the transverse conductivities, image analysis and computations are necessary. The numerical procedure used is based on a change of scale procedure using the Volume Averaging Method. Starting from the equations at a given scale, this method leads to

higher scale equations and closure problems allowing the determination of effective properties. The closure problem obtained for heat conduction is solved numerically with a homemade Finite Volume solver in a 1 voxel-thick 3D periodic unit cell representative of the studied medium, thus leading to the determination of the effective heat conductivity tensor [20]. For a given image, the fiber volume fraction is also assessed. The results are used to yield expressions relating the transverse and parallel conductivities to the local fiber volume fraction.

4.3. Second change of scale based on 3D μCT

The proposed procedure takes into account the true space distribution of phases and orientations, as sampled at the macroscale (see Ref. [19] for details). The hypothesis made is that the phase distribution *vs.* property correlation is correctly sampled at the microscale and directly transposable for macroscale computations. The procedure consists in computing the effective thermal properties of the low-resolution images from a field of small-scale properties by the method of Volume Averaging. It starts with the subdivision of the low-resolution images into sub-images; then, inside every sub-image, an evaluation of fiber volume fraction and local fiber orientation is performed. This part of the algorithm is carried out by binarizing arbitrarily the image at 50% level threshold, letting random walkers run in one of the two phases, computing the variance of their centered displacements, and selecting the eigenvector associated to the highest eigenvalue (*i. e.* the direction of fastest diffusion). Once this has been done, local property tensors may be affected to every sub-image; the values of parallel and perpendicular conductivities come from the results of the first change of scale (see above), as a function of the local grayscale level and the tensors are properly rotated to be expressed in the axes of the sample image considered. Finally a change of scale computation is carried out with the same numerical tool [20] as for the first one.

5. Results

5.1. Experimental

For each sample, the thermal field has been recorded as a function of time. From this thermal field evolution, it is possible to determine the thermal transverse diffusivity (averaged on composite thickness) for each pixel [21,22] (see Fig. 3a,b) and to plot the thermal diffusivity histograms (Fig. 3c). These maps and histograms demonstrate that, though both composites are quite similar in terms of thermal diffusivity magnitude, the chopped one displays more dispersion, as could be expected from its structure.

Moreover, thermal conductivities along transverse and longitudinal directions were measured by the hot disk method. These measurements only concern chopped composites and were done on 4×5 cm^2 samples. The results are in excellent agreement with those obtained through thermography, as can be seen in Table 2. Values are similar to those reported in Ref. [23].

5.2. Numerical results

As already mentioned, the method to calculate the equivalent conductivity tensor is based on 3D μCT images as input geometry of the material. But at the micro-scale, the resolution of μCT images was not sufficient, justifying the use of micrographs. We first present results on 2D micrographs for the first change of scale, and then on 3D μCT scans for the second change of scale.

5.2.1. First change of scale based on 2D imaging

The first change of scale has been performed on micrographs similar to the one presented in Fig. 2d. Four of these images obtained after processing are presented on Fig. 4.

The results of effective conductivity computations were compared to known analytical estimations of the transverse conductivity proposed in the literature. First, the lowest conceivable bound is given by the harmonic average corresponding to the 1D law of conduction in series:

$$\lambda_\perp^{-1} = \phi_f \lambda_f^{-1} + \phi_m \lambda_m^{-1} \tag{2}$$

while the highest bound is given by the arithmetic average corresponding to the 1D law of conduction in parallel. A first more elaborate model has been proposed by Maxwell Garnett [24], in which the thermal conductivity of a regular array of cylinders in a matrix is given as a function of fiber fraction by the following relationship:

$$\frac{\lambda_\perp - \lambda_m}{\lambda_\perp + (d-1)\lambda_m} = \phi_f \frac{\lambda_f - \lambda_m}{\lambda_f + (d-1)\lambda_m} \tag{3}$$

where d is the dimension of the problem. This equation, with $d = 2$, as is the case here, is equivalent to the relation of Hasselman & Johnson [25]. More elaborate relations were proposed by Perrins et al. [26] for a square array of cylindrical fibers:

$$\frac{\lambda_m}{\lambda_\perp} = 1 - \frac{2\phi_f}{F + \phi_f - \frac{0.305827F\phi_f^4}{F^2 - 1.402958\phi_f^8} - \frac{0.013362\phi_f^8}{F}} \tag{4}$$

and for a hexagonal array:

$$\frac{\lambda_m}{\lambda_\perp} = 1 - \frac{2\phi_f}{F + \phi_f - \frac{0.075422F\phi_f^6}{F^2 - 1.060283\phi_f^{12}} - \frac{0.000076\phi_f^{12}}{F}} \tag{5}$$

with $F = \frac{\lambda_m + \lambda_f}{\lambda_m - \lambda_f}$. The comparison of the transverse conductivity *vs.* fiber ratio curves calculated with all these laws and the one obtained by fitting the numerical results is reported in Fig. 4. It can be seen that the relationships of Maxwell Garnett and of Perrins et al. always underestimate slightly (by 5% or less) the computed values. At high fiber volume fractions, the law of Perrins et al. for square arrays of cylinders matches well the numerical data. For the sake of convenience, the transverse conductivity $\lambda_\perp$ has been fitted by the following polynomial law:

$$\lambda_\perp = -2.021932\phi_f^3 + 4.627975\phi_f^2 - 2.202157\phi_f + 0.7120661 \tag{6}$$

5.2.2. Second change of scale based on 3D μCT

The second change of scale is performed on an image of a volume of the material large enough to contain an REV (Representative Elementary Volume). The image is divided into several sub-volumes (see Fig. 5). For each sub-domain, the fibers and matrix are first thresholded to 50% black/50% white, and anisotropy directions are then detected using a random walk algorithm where the walkers are only allowed to travel in one phase. This method, simulating a diffusion process in the image, is sensitive to its local structure. The analysis of eigenvectors and eigenvalues of the covariance tensor of the relative walkers' displacements gives the fiber direction in the sub-volume: the direction associated to the highest eigenvalue is the average fiber direction. This procedure has
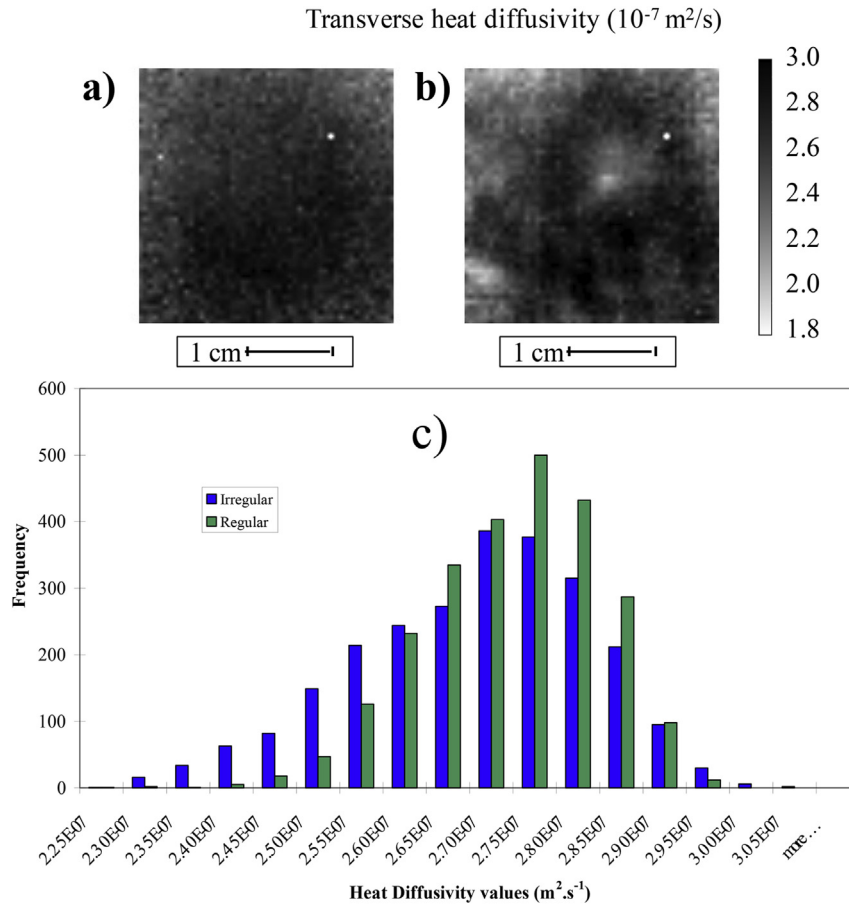
Fig. 3. Heat diffusivity maps from the flash experiments on a) plain woven composite (regular) and b) chopped fabric composite (irregular). c) Histograms of thermal diffusivity of both composites.

Table 2
Thermal properties of regular and chopped composites.

| Property	Regular	Chopped	Method
Specific volume heat ($J/cm^3/K$)	1.70 ± 0.01	1.63 ± 0.03	DSC
Transverse thermal diffusivity (mm^2/s)	0.28 ± 0.01	0.27 ± 0.01	Flash + IR cameraFlash + Degiovanni
	0.27 ± 0.01	0.26 ± 0.01	Hot disk
	−	0.26 ± 0.01	
Longitudinal thermal diffusivity (mm^2/s)	0.33 ± 0.01	0.31 ± 0.01	Flash + Degiovanni
	−	0.31 ± 0.01	Hot disk
Transverse thermal conductivity (W/m/K)	0.45 ± 0.02	0.44 ± 0.02	Diffusivity × spec. heat
Longitudinal thermal conductivity (W/m/K)	0.56 ± 0.02	0.51 ± 0.02	Diffusivity × spec. heat
Transverse thermal conductivity (W/m/K)	0.47	0.45	Computed
Longitudinal thermal conductivity (W/m/K)	0.54	0.51	Computed

been successfully validated on μCT images of C/C composites [19,27].

In addition to this, a correspondence between the average gray scale value of the sub-domain and its local values of the fibers, pore, and matrix volume fractions is provided through the choice of correlation functions. As sketched in Fig. 6, the gray scale histograms of the images can be modeled using two Gaussian functions: the first one corresponds to the inter-yarn material (*i.e.* principally matrix), the second one to the yarns themselves. The mode N2 of the first Gaussian corresponds to the matrix density and the mode N3 of the second one corresponds to the average density of yarns, *i.e.* of a material with fiber density corresponding to the volume fraction of fibers in the yarn, $\phi_{f,yarn}$, and matrix density corresponding to $\phi_{m, yarn} = 1 - \phi_{f,yarn}$, since there are no intra-yarn pores.

Between N2 and N3, a linear interpolation is made, and it is prolonged until the fiber volume fraction reaches 1. The pores are obtained by direct thresholding of the image, with a threshold value N1 chosen so that the experimental porosity is recovered.

Using this information and the correlations obtained from the first change of scale, longitudinal and transverse thermal conductivities are computed. For each sub-volume, a diagonal thermal conductivity tensor is allocated in its own principal directions then rotated back in the image's global frame [19]. The effective macroscopic conductivity tensor is then obtained from the data of all sub-domains by solving the closure problem associated to the Volume Averaging Method, using the same solver as for the first change of scale [20].

Macroscopic conductivity tensors, $\underline{\lambda}^*$, for both composites,
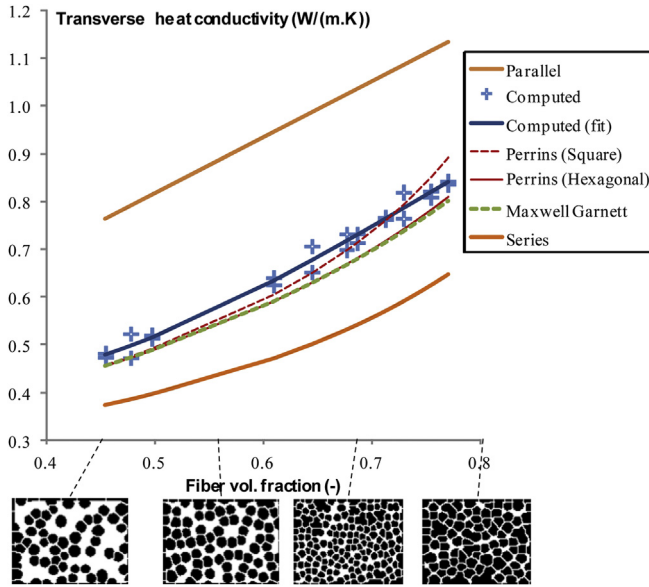
Fig. 4. Transverse conductivity *vs.* fiber ratio calculated by change of scale (crosses: numerical, thick continuous line: polynomial fit), by several laws from literature (dashed lines), and by the series and parallel conduction bounds (upper and lower continuous curves). Extracts of micrographs (scale ×50) of 4 fields of fibers taken at different locations and processed as described in the text are shown below. Black pixels lie in fibers, white ones in the matrix.
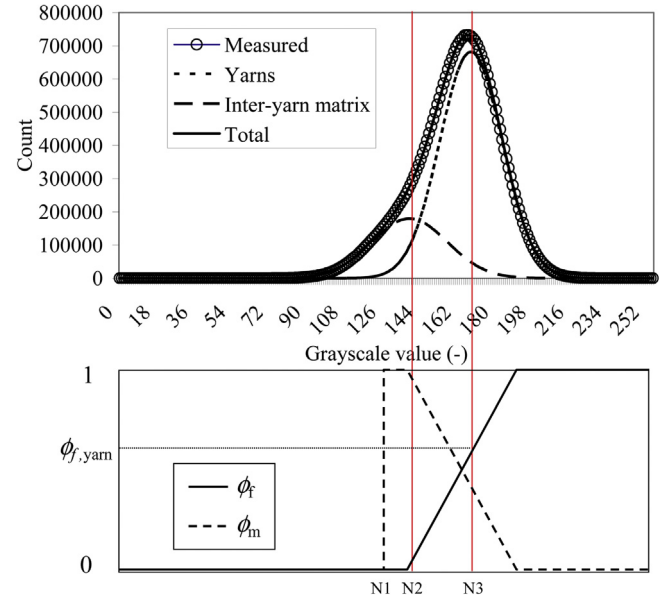
Fig. 6. Above: histogram of the original image, with two fitted Gaussians, one related to the matrix, the other one to the yarns. Below: computation of the fiber and matrix volume fractions as a function of the grayscale level.
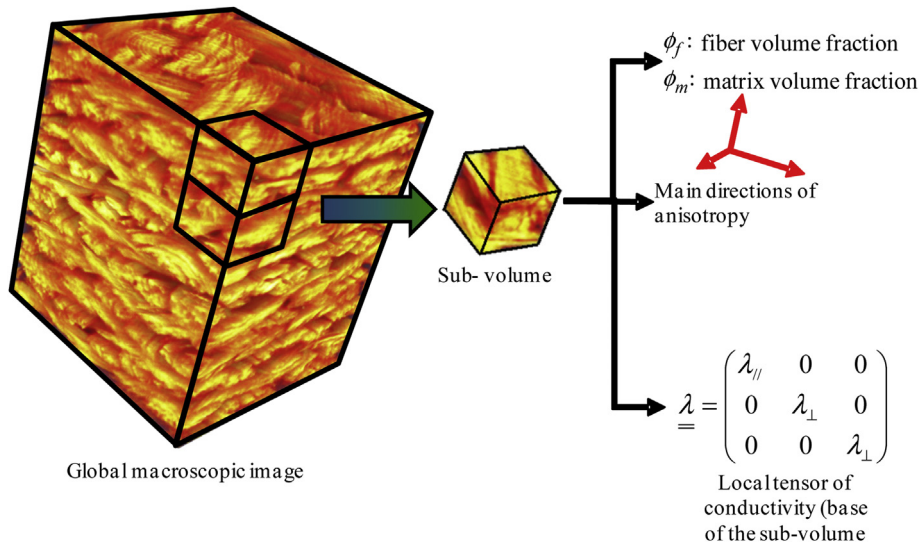
Fig. 5. Illustration of the computations for each subdomain prior to the second change of scale.

obtained thanks to this double change of scale method, on the 3D blocks shown in Fig. 1c,d, are respectively

$$\underline{\underline{\lambda}}^* = \begin{pmatrix} 0.5381 & 0.0089 & -0.0007 \\ 0.0090 & 0.5381 & 0.0027 \\ -0.0007 & 0.0027 & 0.4730 \end{pmatrix} \quad (7)$$

for the regular composite and

$$\underline{\underline{\lambda}}^* = \begin{pmatrix} 0.5037 & -0.0047 & -0.0047 \\ -0.0047 & 0.5260 & -0.0036 \\ -0.0047 & -0.0036 & 0.4495 \end{pmatrix} \quad (8)$$

for the chopped composite.

6. Discussion

For both regular and chopped composites, the non-diagonal terms in the conductivity tensors reported in Eqs. (7) and (8) are negligible: directions x, y and z of the tomographic image match those of thermal conduction. Comparing with flash thermography results, for the regular composite, it can be noted that longitudinal conductivity (directions x and y with similar values) is, as in experiments, higher than the conductivity in the z direction. The agreement in both directions is excellent. The same tendency is obtained for the chopped composite. For this material, the computed λ^*_{xx} and λ^*_{yy} differ by 5%, indicating that the area selected for computation was somewhat too small with respect to an REV

Table 3
Normalized sensitivities of the computed macroscopic thermal conductivities to different parameters.

Normalized sensitivities to:	Regular		Chopped	
	Longitudinal	Transverse	Longitudinal	Transverse
λ_f	0.70	0.64	0.68	0.61
λ_m	0.50	0.55	0.52	0.56
N1	0.12%	0.13%	0.11%	0.13%
N2	0.9%	1.0%	0.9%	1.0%
N3	0.9%	1.0%	0.9%	1.0%

size. However, the computed value of transverse conductivity is, as in experiments, lower than longitudinal ones. The average computed longitudinal value matches the measured value within the error bounds.

The thermal anisotropy can be conveniently quantified by the following parameter:

$$\tau = \frac{\lambda_{//}^* - \lambda_{\perp}^*}{\lambda_{//}^*} \qquad (9)$$

Experimentally, we obtained anisotropies of 19.6% ± 7% and 13.7% ± 1% respectively for the regular and chopped composites, while the computations give values of 12% and 10% respectively, that is, somewhat too low, especially for the regular composite. Despite these remarks, the image-based computational procedure has shown its ability to successfully reproduce the effect of the reinforcement arrangement on heat conduction.

The numerical procedure has been repeated with small variations of the fiber and matrix conductivities, and of the grayscale levels used in the thresholding procedure, in order to obtain the respective normalized sensitivities $S_{\lambda i} = \partial \ln \lambda^* / \partial \ln \lambda_i$ ($i = f$ or m) and $S_{Ni} = \partial \ln \lambda^* / \partial Ni$ ($i = 1, 2$ or 3), as reported in Table 3. The sensitivity with respect to matrix or fibers conductivity lying respectively around 0.5 (matrix) and 0.7 (fiber), we conclude that a small error in the knowledge of these constituent properties has no catastrophic effect on the computational predictions (a 1% variation in λ_m gives a 0.5% variation in λ^*). In the same manner, the threshold N1, though important for correct density determinations, has a very low impact on the effective conductivity. On the other hand, the method is more sensitive to the N2 and N3 levels chosen for the grayscale/density conversion function. A variation of 1 gray level of N2 or N3 implies a variation of about 1% in λ^*. Since these parameters are obtained from the knowledge of the fiber and matrix volume fractions, the experimental determination of the latter quantities is the most critical point of the procedure.

7. Conclusion

This paper has presented a study of a silica/phenolic composite family based on two main approaches: (*i*) the measurement of thermal and structural properties through various experiments, and (*ii*) a double-step computational change of scale. The latter approach is based on 2D and 3D images of the microstructure of the composites. Using the properties of the constituents and their relative spatial organization, the approach yields effective conductivities of the composite.

The numerical results are in good agreement with experiments and can be easily applied to fiber-reinforced composites in general, using microscopic images and tomographic scans. Improvements are now necessary to optimize the change of scale routine calculation in terms of computational time.

The two composites with different spatial organizations have been found to have very close thermal conductivities in different directions. The transverse conductivities of the chopped composite display more dispersion on the plate, as expected from its structure. This may have a positive impact on ablation resistance; indeed, exposed to the same heat flux, the heat penetration depth will be more dispersed, resulting in a wavier pyrolysis front. The heat consumption by pyrolysis will therefore increase by the ratio of the actual surface to the projected surface, and will bring a better protection.

References

[1] Laub B, Venkatapathy E. Thermal protection system technology and facility needs for demanding future planetary missions. In: Wilson A, editor. Procs. Intl. Workshop on planetary probe atmospheric entry and descent trajectory analysis and science. Netherlands: ESA Publications Division; 2004. p. 239–47. ESA Confs. Procs. SP-544, Noordwijk.

[2] Dauchier M, and Cavalier J.-C. Matériaux composites phénoliques ablatifs, Tech de l'Ingénieur 2002, Paris: Editions TI, ref. AM 5325 (in French). http://www.techniques-ingenieur.fr/base-documentaire/materiaux-th11/materiaux-composites-presentation-et-renforts-42142210/materiaux-composites-phenoliques-ablatifs-am5325/M.

[3] Sykes GF. Decomposition characteristics of a char-forming phenolic polymer used for ablative composites. Technical Note NASA TN D3810. 1967.

[4] Kanno Y. Development of ablative material for planetary entry. In: Miravete A, editor. Procs. 9th international conference on composite materials vol. VI — composites: properties and applications. Zaragoza University & Woodhead Publishing; 1993. p. 120–4.

[5] Gregori ML, Barros EA, Petraconi Filho G, Costa SF. Mechanical and ablative properties of silica-phenolic composites for thermal protection. In: Weihs H, Herdrich G, Ritter H, editors. Procs. 6th eur. Workshop on TPS and hot structures; 2009.

[6] Gregori ML, Barros EA, Petraconi Filho G, Pardini LC, Costa SF. Ablative and mechanical properties of quartz phenolic composites. J Aerosp Technol Manag 2009;1(1):63–8.

[7] Sohn MS, Hu XZ. Mode II delamination toughness of carbon-fibre/epoxy composites with chopped kevlar fibre reinforcement. Compos Sci Technol 1994;52(3):439–48.

[8] Greenhalgh E, Hiley M. The assessment of novel materials and processes for the impact tolerant design of stiffened composite aerospace structures. Compos Part A App Sci Manuf 2003;34(2):151–61.

[9] Ramesh Kumar R, Vinod G, Renjith S, Rajeev G, Jana MK, Harikrishnan R. Thermo-structural analysis of composite structures. Mater Sci Eng A 2005;412(1–2):66–70.

[10] Vignoles GL, Bresson G, Lorrette C, Ahmadi-Sénichault A. Measurement of the thermal diffusivity of a silica fiber bundle using a laser and an IR camera. J Phys Conf Ser 2012;395:012079 (7 pp.).

[11] Degiovanni A. Diffusivité thermique et méthode flash. Rev. Gén. Therm. 1977;185:420–42 (in French).

[12] Parker WJ, Jenkins J, Butter CP, Abbot GL. Flash method of determining thermal diffusivity, heat capacity, and thermal conductivity. J Appl Phys 1961;32(9):1679–84.

[13] Gustavsson M, Karawacki E, Gustafsson SE. Thermal conductivity, thermal diffusivity and specific heat of thin samples from transient measurement with Hot Disk sensors. Rev Sci Instrum 1994;65(12):3856–9.

[14] Gustavsson M, Gustafsson SE. On the use of transient plane source sensors for studying materials with direction dependent properties. In: Dinwiddie RB, editor. Procs. Thermal conductivity 26-Thermal expansion 14, joint conferences 2001. Lancaster, PA: DESTech Publications; 2005. p. 367–77.

[15] Rasband WS. ImageJ software. Bethesda, Maryland, USA: U.S. National Institute of Health; 1997–2014. Consulted June 10, 2014, http://imagej.nih.gov/ij/.

[16] Maire E, Buffière J-Y, Salvo L, Blandin JJ, Ludwig W, Létang JM. On the application of X-ray microtomography in the field of materials science. Adv Eng Mater 2001;3(8):539–46.

[17] Herman GT. Image reconstruction from projections. New York: Academic Press:; 1980.

[18] Feldkamp LA, Davis LC, Kress JW. Practical cone-beam algorithm. J Opt Soc Am A 1984;1(6):612–9.

[19] Vignoles GL, Coindreau O, Ahmadi A, Bernard D. Assessment of geometrical and transport properties of a fibrous C/C composite preform as digitized by X-ray computerized microtomography: Part II. Heat and gas transport properties. J Mater Res 2007;22(6):1537–50.

[20] Lux J, Ahmadi A, Gobbé C, Delisée C. Macroscopic thermal properties of real fibrous materials: volume averaging method and 3D image analysis. Int J Heat Mass Transf 2006;49(11–12):1958–73.

[21] Bamford M, Florian M, Vignoles GL, Batsale J-C, Alves Cairo CA, Maillé L. Global and local characterization of the thermal diffusivities of SiC$_f$/SiC composites with infrared thermography and flash method. Compos Sci Technol 2009;69(7–8):1131–41.

[22] Bamford M, Batsale J-C, Fudym O. Nodal and modal strategies for longitudinal thermal diffusivity profile estimation: application to the non-destructive evaluation of SiC/SiC composites under uniaxial tensile tests. Infrared Phys Technol 2009;52(1):1–13.

[23] Mottram JT, Taylor R. Thermal conductivity of fibre-phenolic resin composites. Part I. Thermal diffusivity measurements. Compos Sci Technol 1987;29(3): 189–210.

[24] Maxwell Garnett JC. Colors in metal glasses and in metallic films. Philos Trans R Soc Lond 1904;203:2083–92.

[25] Hasselmann DPH, Johnson LF. Effective thermal conductivity of composites with interfacial thermal barrier resistance. J Compos Mater 1987;21(6): 508–15.

[26] Perrins WT, McKenzie DR, McPhedran RC. Transport properties of regular arrays of cylinders. Proc R Soc Lond A 1979;369:207–25.

[27] Coindreau O, Vignoles GL. Assessment of structural and transport properties in fibrous C/C composite preforms as digitized by X-ray CMT. Part I : image acquisition and geometrical properties. J Mater Res 2005;20(9):2328–39.